FINE AND COARSE DUST RADIATIVE IMPACT DURING AN INTENSE SAHARAN DUST OUTBREAK OVER THE IBERIAN PENINSULA. PART I: SHORT-WAVE DIRECT RADIATIVE EFFECT

5   María-Ángeles López-Cayuela[1], Carmen Córdoba-Jabonero[1*], Michaël Sicard[2,#], Jesús Abril-Gago[3,4], Vanda Salgueiro[5,6], Adolfo Comerón[2], María José Granados-Muñoz[3,4], María João Costa[5,6], Constantino Muñoz-Porcar[2], Juan Antonio Bravo-Aranda[3,4], Daniele Bortoli[5,6], Alejandro Rodríguez-Gómez[2], Lucas Alados-Arboledas[3,4], and Juan Luis Guerrero-Rascado[3,4]

10   [1]Instituto Nacional de Técnica Aeroespacial (INTA), Atmospheric Research and Instrumentation Branch, Torrejón de Ardoz, 28850-Madrid, Spain
[2]CommSensLab, Dept. of Signal Theory and Communications, Universitat Politècnica de Catalunya (UPC), 08034-Barcelona, Spain.
[3]Andalusian Institute for Earth System Research (IISTA-CEAMA), 18006-Granada, Spain
15   [4]Department of Applied Physics, University of Granada (UGR), 18071-Granada, Spain
[5]Institute of Earth Sciences (ICT) and Earth Remote Sensing Laboratory (EaRSLab), Évora, Portugal
[6]Department of Physics, University of Évora, 7000-671, Évora, Portugal
[#]Now at: Laboratoire de l'Atmosphère et des Cyclones (LACy), Université de La Réunion, Saint Denis, France

Correspondence to: Carmen Córdoba-Jabonero (cordobajc@inta.es)

20   **Abstract.** Mineral dust has a key role in the Earth's radiative balance, and it has become significant over the Iberian Peninsula (IP), where Saharan dust outbreaks seem to increase in frequency and intensity. This study quantifies the dust direct radiative effect (DRE) in the short-wave range (SW), during an intense persistent springtime dust episode over the IP. A long-term analysis (14 days) was performed over five lidar stations. The vertical distribution of dust optical properties was derived, finding a wide dynamic range of aerosol concentration that allowed a suitable statistical study. The Global Atmospheric Model

25   (GAME) was used for radiative transfer simulations. This study innovates by simulating the SW DRE using two distinct methodologies, finding differences between both approaches. The novel approach separates the impact of both fine (Df) and coarse (Dc) dust components and calculates the total DRE as their combined sum. In contrast, the approach commonly used directly simulates the DRE for the total dust as a whole. Across the dust pathway along the IP, the SW DRE consistently registered a pattern of aerosol-induced cooling at both surface (BOA) and top-of-the-atmosphere (TOA). Results agree with

30   the fact that the Df role cannot be disregarded, that is primarily responsible for SW radiative modulation. In particular, Df contributed nearly half of the total DRE at BOA and TOA in this event. In addition, the Df-to-total ratio influences the differences in DRE obtained by comparing both methodologies, being higher when the differences of the asymmetry factor at 440 nm between the fine and total dust component are greater than a value of 0.1.

1 Introduction

35 According to the latest Intergovernmental Panel on Climate Change technical report (IPCC, 2023), not only is the Earth's global average temperature rising, but an increase in the frequency, intensity, and duration of extreme hot events and extreme precipitation has also been observed over several zones in the last few years. In this context of climate change, aerosols play a crucial role in climate forcing, both through their direct impact by interacting with radiation (aerosol-radiation interactions, ARI) and their indirect effect by serving as cloud condensation nuclei and ice nucleating particles (aerosol-cloud interactions,

40 ACI). From 1750 to 2014, aerosols contributed to the global effective radiative forcing at the top of the atmosphere (TOA) by -1.3 W m-2, resulting in a cooling effect (Arias et al., 2021), which partially compensates for the warming effect by increasing greenhouse gas emissions.

Among aerosol particles, mineral dust is one of the most abundant and widely distributed in the Earth's atmosphere. Significant uncertainties remain in the estimation of the dust radiative effect, mostly because of the lack of observational constraints in

45 dust interactions with clouds, among other factors (Kok et al., 2023). In particular, the Sahara desert and Sahel regions are the major contributors to mineral dust lifting, accounting for over 50 % of global emissions (Kok et al., 2021). The geographical proximity of the Iberian Peninsula (IP) to North Africa, as well as the persistence of certain favourable weather patterns (Russo et al., 2020; Couto et al., 2021), make the IP one of the main pathway regions for desert dust transport towards Europe. Indeed, there is robust evidence for increases in maximum temperatures and the frequency of heatwaves over Europe (IPCC, 2023),

50 partially associated with dust intrusions. While there are certain indications that future global dust aerosol concentrations may increase (Allen et al., 2016; Tegen and Schepanski, 2018), this likelihood is notably contingent upon alterations in precipitation patterns and atmospheric circulation (IPCC, 2023). Consequently, the radiative consequences of such potential changes remain unclear (Allen et al., 2016; Kok et al., 2018). Since pre-industrial times, the dust mass that has lifted into the atmosphere in those North African regions has increased by 46% (Kok et al., 2023). Moreover, there is not only an increasing frequency of

55 Saharan dust outbreaks over the IP, when compared with long-term records (Sousa et al., 2019; Salvador et al., 2022), but also in the number of studies reporting extreme and intense dust episodes in the region (e.g. Guerrero-Rascado et al., 2009; Preißler et al., 2011; Santos et al., 2013; Cazorla et al., 2017; Sorribas et al., 2017; Titos et al., 2017; Valenzuela et al., 2017; Córdoba-Jabonero et al., 2019, 2021; Fernández et al., 2019; López-Cayuela et al., 2023).

This study focuses on the interaction of Saharan dust with radiation, i.e., on the direct radiative effect (DRE) of dust particles.

60 By using observational measurements, the estimation of the DRE is performed, underscoring the importance of determining their radiative properties and accurately quantifying their direct radiative impact on the Earth-atmosphere radiative budget. This work aims to study the DRE during an exceptionally intense and long-lasting (14 days, from 25 March to 7 April 2021) Saharan dust event over the IP, allowing a long-term study of changes in the radiative properties across both temporal and spatial dimensions. This event was well characterized in the work of López-Cayuela et al. (2023) by determining the vertical

65 behaviour of the optical and microphysical dust properties and using data obtained from five Iberian lidar stations. This study focuses on the direct radiative effect of the dust particles in the short-wave (SW) spectral range.

2

The use of lidar measurements should be emphasised as an added value of this study. Thanks to the application of the POLIPHON algorithm (Polarisation Lidar photometer Networking method; Mamouri and Ansmann, 2014, 2017; Ansmann et al., 2019) to the polarized lidar measurements, it is possible to separate the fine and coarse dust contributions (Df and Dc,

70 respectively) to the total DRE. In this work, the Df particle role has been highlighted in contrast to most part of the studies, in which the potential impact of Df particles on the total radiative effect has been mostly ignored. The reason for overlooked Df contribution is that dust intrusions are typically dominated by large particles (Dc), in particular, near the source. Indeed, the DRE of total dust (DD) has been extensively studied in both SW and LW spectral ranges (e.g. Sicard et al., 2014a, 2016; Barragán et al., 2016; Granados-Muñoz et al., 2019) but only a few studies have addressed this issue by separating both dust

75 components. For instance, Sicard et al. (2014b) reported that Dc particles primarily affect LW solar radiation, while Df is primarily responsible for SW radiative modulation. Furthermore, the impact of Df particles in the SW spectral range of the solar radiation is greater at the top-of-atmosphere (TOA) than at the surface (BOA) (Córdoba-Jabonero et al., 2021), while the contribution of the Dc particles in the LW solar spectral range at the TOA is lesser than at the BOA (Sicard et al., 2022). Hence, we consider that it is essential to study both Df and Dc particles separately when estimating individual radiative effects.

80 As an added value, this study introduces the novelty of simulating SW dust DRE using two distinct approaches to assess if significant differences between both methodologies can be found. On the one hand, by simulating the contribution of Df and Dc components separately, and then estimating the total dust DRE as their sum (DD = Df + Dc). On the other hand, the DRE is directly simulated for the total dust component.

The paper is organized as follows. The GAME radiative transfer model and the parametrizations used in terms of SW range

85 are described in Section 2. An overview of the dust outbreak can be found in Section 3. In Section 4 the results and discussion are exposed. Finally, the main conclusions of this study are found in Section 5.

2. Methodology: solar radiation simulations

2.1 Radiative transfer model: GAME

GAME (Global Atmospheric Model) is the radiative transfer model (RTM) used in this study for computing the solar radiation

90 fluxes. Particularly in this work, they are simulated in the SW spectral range (0.2 to 4.0 μm, with a wavenumber resolution of 400 cm^{-1} from 0.2 to 0.7 μm and 100 cm^{-1} from 0.7 to 4.0 μm). Hereafter, for simplicity, the 'SW' notation is omitted. GAME was developed by Dubuisson et al. (1996, 2004) and employs the discrete ordinates method (DISORT; Stamnes et al., 1988) to compute the solar flux at the boundary of homogenous and plane atmospheric layers. The SW radiation flux is calculated for 18 layers of the atmosphere ranging from ground level to an altitude of 20 km height.

95 This RTM accounts for the absorption of gases, specifically H_2O, CO_2, O_3, N_2O, CO, CH_4, and N_2, using the correlated k distribution (Lacis and Oinas, 1991). Additional information on the calculation of the gas transmission functions can be found in Dubuisson et al. (2004) and Sicard et al. (2014b). The parameterization of gas absorption is based on pressure, temperature, and relative humidity profiles. Particularly, the data from the Global Data Assimilation System (GDAS), provided by the

3

National Oceanic and Atmospheric Administration (NOAA) are used (ftp.arl.noaa.gov/archives/gdas1/; last access: 28

100 February 2023). Additionally, the model requires input from the spectrally resolved surface albedo (SA), whose data are

obtained from MODIS (Moderate Resolution Imaging Spectrometer; https://modis.gsfc.nasa.gov; last access: 28 March 2023).

In GAME model, aerosols are included by comprehensively parameterizing their radiative properties in terms of the spectral

dust extinction coefficient (α), single scattering albedo (ω), and asymmetry factor (g). Both ω and g values are assumed to be

vertically constant, and equal to the columnar values of ω and g, as taken from NASA's AERONET (AErosol RObotic

105 NETwork; http://aeronet.gsfc.nasa.gov) Version 3 Level 2.0 data inversion products (last access: 18 February 2023). They are

interpolated at the model wavelengths up to the largest SW wavelength provided by AERONET (1020 nm) and assumed to be

constant beyond. In addition, they are hourly averaged, and interpolated in case those hourly values are missing. Also note that

g is given separately for the fine, coarse and total modes. At the time of writing this study, fewer or no AERONET Level 2.0

data were available for all the stations. In such cases, AERONET Level 1.5 data were used instead. Those AERONET g and

110 ω are given with an uncertainty of ±0.03 and ±0.04, respectively, for dust particles (Dubovik et al., 2000, 2002).

The vertical profiles of the dust extinction coefficient at 532 nm (α^{532}) for both the coarse- and fine- modes were previously

obtained in López-Cayuela et al. (2023). As described in that work, the α retrieval was performed by applying the POLIPHON

method (Mamouri and Ansmann, 2017; Córdoba-Jabonero et al., 2018) to the continuous hourly-averaged lidar measurements

and in this work, they have been degraded to the 18 model layers, ranging from the surface up to 20 km height. In addition,

115 the lidar-derived α^{532} profiles are used together with the AERONET Ångström exponent at 440-870 nm (AE[440-870]) to derive

the height-resolved dust extinction at other wavelengths within the SW range. Hourly dust optical depth (DOD) values for

both modes and for the total dust (DD) are computed by integrating those spectrally-estimated dust extinction coefficient

profiles.

The input parameters and radiative properties as introduced in the GAME model for the SW spectral range and the databases

120 used are summarized in Table 1.

2.2 Dust radiative effect estimation

The aerosol direct radiative effect (ARE) is particularly obtained for dust as the dust direct radiative effect (DRE), which can

be defined at a given height (z) as follows (Córdoba-Jabonero et al., 2021; Sicard et al., 2022),

$$DRE(z) = \left[F_d^\downarrow(z) - F_d^\uparrow(z) \right] - \left[F_0^\downarrow(z) - F_0^\uparrow(z) \right], \tag{1}$$

125 where F_d and F_0 denote the solar radiative flux (W m^{-2}) as computed by GAME, respectively, with (d) and without (0) dust

occurrence. The ↓ and ↑ arrows indicate whether the fluxes are downward or upward, respectively. The first ($\left[F_d^\downarrow(z) - F_d^\uparrow(z) \right]$)

and second ($\left[F_0^\downarrow(z) - F_0^\uparrow(z) \right]$) terms of Equation (1) represent, respectively, the net flux with and without dust presence.

According to that definition, a negative/positive DRE value would represent a cooling/warming effect. In this study, the DRE

is shown at both TOA and BOA. The dust contribution in the overall atmospheric column is evaluated by quantifying the

130 atmospheric radiative effect, DRE(ATM), which is defined as follows,

4

$$DRE(ATM) = DRE(TOA) - DRE(BOA), \qquad\qquad (2)$$

Note that α profiles are obtained from 'hourly' lidar measurements, and the DRE values denote 'instantaneous' simulated radiative values as obtained from those hourly α profiles; hence, for simplicity, both terms are removed. The fine-to-total ratio (Df/DD) of DRE (ftr_DRE) is also calculated, together with a linear fitting analysis of that variable over time. The slope of

135   this linear fitting, denoted as δDRE, represents a measure of the temporal rate of the relative Df contribution to the DRE. Besides, the daily-averaged DRE is computed as follows:

$$DRE^{daily} = \frac{N_d}{24}\frac{\sum_{i=1}^{N} DRE^{hourly}}{N}, \qquad\qquad (3)$$

where N is the number of hourly DRE values as computed for each day, and N_d is the total number of hours with solar zenith angles (SZA) < 90° along the day (i.e. N_d = 12 in this work). Moreover, the episode-averaged DRE is computed as the average

140   of the daily-averaged DRE values for the entire event. For simplicity, hourly DRE will be denoted by DRE hereafter, if unless otherwise specified.

The dust radiative efficiency (DREff) is defined as the ratio of the DRE to DOD^{532} values along the day. Hence, the daily DREff is obtained from the slope of their linear fitting of DRE values with respect to DOD^{532}, forced to zero for each day.

In addition, an analysis is performed by comparing the dust-induced DRE as obtained from two approaches:

145   1)   the previously exposed one, i.e., considering the contribution of the Df and Dc particles separately in the DRE, following the expression below:

$$DRE^{(I)} = DRE^{DD} = DRE^{Df} + DRE^{Dc}, \qquad\qquad (4)$$

        2)   DRE is obtained from the contribution of the total dust in overall,

$$DRE^{(II)} = DRE^{total}, \qquad\qquad (5)$$

150   For that purpose, differences found in the dust-induced DRE (ΔDRE) between the two approaches are expressed as:

$$\Delta DRE = DRE^{(I)} - DRE^{(II)}, \qquad\qquad (6)$$

That notation will be employed throughout the entire paper. That is, 'DD' will refer to variables obtained by summing Df and Dc variables, and 'total dust' will denote variables obtained without considering the mode separation. Note that the second approach ($DRE^{(II)}$) is the most used in the literature. In this study, the first approach ($DRE^{(I)}$) could be considered more precise,

155   as it enables the characterization of the optical properties of each dust mode separately (Sicard et al., 2014b; Córdoba-Jabonero et al., 2021; Sicard et al., 2022). However, it should be considered that $DRE^{(I)}$ is calculated assuming that the dust-induced diffuse radiation from one of the modes does not interact with the other one.

3. Overlook of the dust outbreak crossing the Iberian Peninsula

During spring 2021, the IP experienced a significant and prolonged dust intrusion (25 March – 7 April). This event was closely

160   monitored and analysed by five lidar stations strategically located across the IP, namely El Arenosillo/Huelva (ARN), Granada

5

(GRA), Torrejón/Madrid (TRJ), and Barcelona (BCN) in Spain, and Évora (EVO) in Portugal. Figure 1 shows the geographical position of each station in the IP.

A deep analysis of the synoptic situation and back-trajectory analysis revealed that the dust intrusion originated in the Saharan region and traversed the IP from the southwest to the northeast. The dust event was accompanied by an extended cloud cover

165 across all five Iberian lidar stations, resulting in the unavailability of some lidar retrievals. Consequently, the dataset exhibits certain gaps, along with periods of no lidar measurements. However, almost 600 cloud-screening day and night lidar profiles were retrieved over the five lidar stations, corresponding almost 60% of them to daytime periods, and used to compute DRE (SZA < 90º, see Sect. 2.2).

The extensive study of the dust outbreak can be found in López-Cayuela et al. (2023), together with the methodology to obtain

170 the optical and mass properties derived from the polarized lidar measurements. This section aims to summarise the most significant results for the optical properties, which are essential for the development and discussion of the current study.

This dust event is particularly noteworthy not only due to the intensity of the dust outbreak but also because the prevailing meteorological situation conditioned the main findings. Among those, there were: 1) the detection of dust in the upper layers of the troposphere on the northern half of the IP (reaching up to 10 km height), caused by the atmospheric instability that

175 induced vertical motions of the air parcels, and 2) the absence of dust ageing observed throughout the IP, which contrasts with the long-range dust events observed in central Europe. In this context, dust ageing is defined as the absence of a uniform gravitational settling of both the coarse and fine dust particles during their transport across the IP.

An overview of the temporal evolution of the dust outbreak crossing the IP in terms of the extinction (α, km^{-1}) over the five Iberian lidar stations is shown in Figure 2. Particularly, the hourly-mean DD α at 532 nm (α_{DD}^{532}) are shown. Despite some

180 data gaps due to either no inversion possible or no lidar measurements, the transport of dust particles can be appreciated by looking at the behaviour of α_{DD}^{532} along the south-west IP (Fig. 2e) to the north-east IP (Fig. 2a) pathway of the dust intrusion during the overall dusty period (25 March – 7 April 2021). In terms of the episode-averaging, DD DOD^{532} decreases as latitude increases, particularly ranging from 0.34 at ARN to 0.14 at BCN, without significant differences in the Df/DD ratio (ftr_DOD) between the stations (approximately 30%, see Table 2).

185 In this work, the hourly-averaged DOD^{532} values are considered low when DOD^{532} < 0.20, moderately intense when 0.2 ≤ DOD^{532} < 0.50, intense when 0.50 ≤ DOD^{532} < 1.00 and extreme for DOD^{532} ≥ 1.00. This episode presented a wide range of DOD^{532} values, allowing a suitable statistical study. It should be highlighted high and extreme DD DOD^{532} values on the days of maximal incidence (29 March – 1 April). The mean and maximum hourly-averaged DOD^{532} values for Df, Dc and DD components during the entire episode are shown in Table 2.

190 **4. Results and discussion**

This section is divided into an analysis of the specific radiative dust properties introduced in the model (Sect. 4.1), the DRE as estimated considering approach 1 (Sect. 4.2), and the discrepancies found by estimating the DRE from the two considered

approaches (Sect. 4.3). GAME calculations are performed when the Sun is above the horizon (SZA < 90°). The DRE is calculated by using Equations (1) and (2), separately for the Df, Dc and total dust components (see Sect. 2.2).

4.1 Dust radiative properties

For each station considered in this study, taking the SA values corresponding to the dust episode, a symmetric distribution is observed (regardless of the wavelength under consideration). In fact, for each wavelength, the relative differences in SA throughout the episode at the same station are less than 0.1%. For this reason, although hourly values are considered for the simulations, Figure 3a represents the mean value of SA per wavelength and station. Conducting the same analysis for the parameters g and ω, a skewed distribution is obtained for each station and wavelength, with maximum relative differences during the dust episode of 1.5 and 2.5%, respectively. For this reason, and although once again the hourly-averaged value of these variables is used for each simulation, Figures 3b-3c depict an hourly data snapshot from the days of highest incidence, i.e., 1 April at 10 UTC for BCN station and 31 March at 12 UTC for the rest of the sites. The g and ω histograms for the five lidar stations can be found in the Supplementary Material (Figs. S1-S5).

Regarding the SA values (Fig 3a), a similar pattern across all sites is found, with SA increasing with wavelength until 870 nm, reaching the maximum values at that wavelength. Within the visible range (VIS, wavelengths < 780 nm) the values increase with latitude, showing $SA^{480} = 0.04$ at ARN and $SA^{480} = 0.07$ at BCN. This characteristic is not preserved at the Near-Infrared range (NIR, 780-2500 nm). EVO and TRJ shows maximum SA values of 0.33-0.36 at 870 nm, which ranges from 0.26 to 0.20 for the other stations. Along the rest of the NIR range, the SA values decrease until $SA_{max}^{2130} = 0.13$-0.18. Notably, the SA values in this study align with those found in Granados-Muñoz et al. (2019) and Córdoba-Jabonero et al. (2021) for GRA and BCN, respectively, in summertime.

Larger SA values indicate that, at a given wavelength and constant incoming radiation reaching the surface, more radiation will be reflected upward. Overall, minimum SA values are found in BCN, while maximum ones are found at TRJ and EVO stations. The differences between the five lidar stations are lower than 5% in the VIS range and for wavelengths greater than 1650 nm. In the beginning of the NIR range (870-1240 nm), EVO and TRJ reflects 7-15% more radiation than the other stations.

Figure 3b and 3c shows the spectral behaviour of g for the fine, coarse and total modes and ω during the most intense days of the episode. Particularly, on 1 April over BCN station and 31 March for the rest of the sites. The results are similar for all the stations, showing typical values expected for dust (Dubovik et al., 2002). Indeed, the differences between the stations are lesser than 5%, regardless of the variable and wavelength being examined.

The g values decrease with the wavelength, being the forward scattering approximately 1.3 times greater for the coarse mode (coarse $g^{440} = 0.82$-0.86) than for the fine mode (fine $g^{440} = 0.67$-0.70). As explained in Córdoba-Jabonero et al. (2021), this result implies that the solar radiation scattered to the surface is greater for the coarse mode than for the fine mode, keeping a constant AOD and at low solar zenith angles (SZA), independently of the wavelength. Regarding the total g, its values range

225   between those for the fine and coarse modes (total g^{440} = 0.75-0.80). The variability of ω is also low between the stations, increasing with wavelength Particularly, ω^{440} ranges from 0.90 to 0.93, being representative of weak absorbing particles. From 675 nm to NIR, ω increases until values of 0.98-0.99 for all stations.

Figure 4 shows the temporal evolution of g^{440} for the fine and coarse components, together with both g^{440} and ω^{440} for the total component at the five lidar stations. Along the entire dust outbreak, these properties remain relatively constant at each

230   station. The variability observed is minimal, with values below 5 and 3% for both g^{440} and ω^{440}, respectively. It should be noted that, in this study, the variability has been quantified as the percentage ratio between the standard deviation and the mean value along the entire episode for each station. Specific values are detailed in Table 3.

As aforementioned, the coarse component of g presents the most influence on scattered radiation. The lowest values of this parameter were observed in ARN and BCN, while the highest values are evident in GRA stations. Thus, the solar radiation

235   scattered to the surface is lower for ARN and BCN than for GRA stations. Conversely, the pattern is reversed for ω. However, it can be considered that the differences among the stations are marginal, displaying relative differences in the episode-average values of less than 3% for the total component in both g^{440} and ω^{440}. Regarding the separation of the dust components, the differences in the episode-averaged g^{440} were 1.5 and 4% for Df and Dc, respectively.

4.2 Dust direct radiative effect

240   Figure 5 shows the temporal evolution of the DRE and the ftr_DRE, at ARN station as an example. To avoid an excessively lengthy paper, the graphics for the rest of the stations can be found in the Supplementary Material (Figs. S6-S9). The episode averaged DRE together with ftr_DRE and δDRE for each station, are shown in Table 4.

4.2.1 DRE at BOA

The DRE is negative at all stations, during the entire dusty period, indicating dust-induced cooling (see Fig. 5a, in purple; for

245   instance, only values are shown for the ARN). The intensity of the episode in terms of the radiative forcing is directly correlated with the DOD^{532}. Thus, during the first part of the episode (until 1 April) the dust event was moderate, showing hourly Df (Dc) DRE values above -10 W m^{-2} (-20 W m^{-2}). During the rest of the episode, the dust event is weaker, showing hourly Df (Dc) DRE values above -5 W m^{-2} (-10 W m^{-2}). However, it should be noted that the event is notably intense at ARN and TRJ stations on some specific days (27 and 31 March, when mean AOD ~ 0.80). In particular, the Df (Dc) DRE reaches hourly values

250   below -40 W m^{-2} (-60 W m^{-2}) at ARN and -20 W m^{-2} (-40 W m^{-2}) at TRJ. Indeed, the maximum hourly DRE for the dust episode is found in ARN (DOD^{532} = 1.30), with extreme values of -54.1 W m^{-2}, (-96.3 W m^{-2}) for Df (Dc) particles. The rest of the stations exhibit maximum values of approximately 30%-50% lower than ARN. Regarding the daily-averaged DRE over all the stations, with low and moderate daily averaged DOD^{532} values (< 0.50) the DRE is ranging from -0.7 W m^{-2} to -11.7 W m^{-2} (-1.6 W m^{-2}, -18.3 W m^{-2}) for Df (Dc) particles. Considering high daily averaged DOD^{532} values (until 1.00), the daily-

255   averaged DRE ranges from -8.7 W m^{-2} to -22.2 W m^{-2} (-18.7 W m^{-2}, -40.6 W m^{-2}) for Df (Dc) particles.

8

For a more accurate comparison between the DRE values found in this work and those reported by other authors, results are compared for those obtained over the IP. Particularly, Córdoba-Jabonero et al. (2021) studied a moderate dust episode over BCN, by separating the Df and Dc component of dust. Maximum DRE values of approximately -22 W m^{-2} (-30 W m^{-2}) for Df (Dc) particles were reported for an hourly averaged DOD^{532} of 0.60. Those maxima values of the present study are nearly 2.5 times greater for an hourly averaged DOD^{532} values 2 times greater than in Córdoba-Jabonero et al. (2021). In addition, the daily-averaged DRE found on this work are similar with those found in Córdoba-Jabonero et al. (2021), for similar daily-averaged DOD^{532} conditions.

The dust-induced DRE as computed in this work is using the approach (I), that is, DRE$^{(I)}$ as the direct sum of the DRE contribution of Df and Dc components (see Sect. 3.2). Thus, the daily-averaged DRE over all the stations ranges (-2.8, -30.0) W m^{-2} for low and moderate DOD^{532} values, and (-27.4, -59.0) W m^{-2} for high DOD^{532} ones. By considering also intense dust episodes over the IP for comparison, Cachorro et al. (2008) reported daily total DRE values of approximately of -107 W m^{-2} at ARN (AOD^{440} = 0.82). In the present work, for similar DOD^{532} values at ARN station, almost half daily DD DRE values (-54.5, -59.0) W m^{-2} were found. Moreover, during a moderate dust outbreak over EVO station (AOD^{440} = 0.48, g^{440} = 0.76), Valenzuela et al. (2017) found daily DRE values of -68.5 W m^{-2}. In this study, for a similar daily-mean DOD^{532} (~ 0.30) and g^{440}, the daily DRE values of (-31.9, -34.1) W m^{-2} are found at the same station, i.e. 50% lower. Finally, for a higher intense dust outbreak over GRA station, Bazo et al. (2023) found daily DRE values of -130.0 W m^{-2} (AOD^{1064} = 1.41, g^{1064} = 0.75), i.e. a 10% greater than the maximum daily DRE values found in this study.

Averaging the daily DRE values over the dust episode (episode-averaged DRE, see Sect. 3.2) could serve as a proxy for understanding the intensity of the overall event. The greatest episode-averaged DRE values for the DD particles are found at GRA, ARN and TRJ, ranging from -5.9 W m^{-2} to -7.1 W m^{-2}, and decreasing 40% at EVO and 50% at BCN. The differences found between stations are mainly related to the DOD decrease with latitude (see Table 2). Indeed, Meloni et al. (2005) found that the radiative forcing at both the TOA and BOA varies almost linearly with AOD and the strong dependence of the DRE on AOD is already well documented (Prasad et al., 2007; Sicard et al., 2014b; Lolli et al., 2018; Meloni et al., 2018; Granados-Muñoz et al., 2019). It is worth noting that the standard deviation of those values at all lidar sites exhibits a similar order of magnitude to the corresponding averages (see Table 4), highlighting the significant variability observed in the dust outbreak, as previously reported by López-Cayuela et al. (2023).

The mean daily ftr_DRE for the entire period (see Table 4) presents similar results at the five lidar stations, being around 40%. This means that Df particles yield almost half of the total DRE at BOA. Regarding the δDRE, a slight increase is observed during the dust outbreak period at each station. This increase can be disregarded, as in any case, it consistently remains below +1% day^{-1} (Fig. 5c, at ARN for instance; Table 4).

Figure 6 shows DRE at BOA (left panels) as a function of DOD^{532}, for instance at ARN (see Fig. 6a-left) for Df, Dc and DD particles, where the DREff values correspond to the slope of the linear fittings for each component. Figure 6a-right shows this analysis for ARN, and Figure 6b-left the DREff values as obtained for all the five lidar stations. Those linear fittings show an excellent degree of confidence, with a correlation coefficient greater than 0.80 in all the stations.

9

290   By averaging those DREff values for the five lidar stations, a mean value of -138.5 ± 20.3 W m^{-2} τ^{-1} (-95.3 ± 5.5 W m^{-2} τ^{-1}) is obtained for Df (Dc) particles. However, by considering the stations separately, the DREff slightly increases with latitude (i.e., from ARN to BCN) up to a maximum of 10% for all particle modes (see Table 4). This behaviour at GRA deserves special mention. Despite being located at a similar latitude as ARN, it exhibits values that are 10% and 5% lower with respect to other stations for Df and Dc particles, respectively. Both ARN and GRA stations present similar g and SA values (see Fig. 3) as

295   well as similar Df/DD proportions, hence the difference may be attributed to the number of data available in this study, triggering a smaller range of DODs at GRA.

For comparison, by considering the fine and coarse modes separately, Córdoba-Jabonero et al. (2021) studied a summer dust outbreak in 2019 over BCN (DD DOD^{532} < 0.6), showing DREff values of -129.6 ± 1.4 W m^{-2} τ^{-1} (-75.2 ± 2.9 W m^{-2} τ^{-1}) for Df (Dc) particles. It implies that the dust event examined in this work shows greater values, with a relative difference of 8%

300   (15%) for Df (Dc) mode with respect to that studied in Córdoba-Jabonero et al. (2021). Other works do not consider both dust contributions separately, so in this part of this work, the DD has been considered for comparison purposes. In the present study, a DREff averaged value of -109.1 ± 7.3 W m^{-2} τ^{-1} was obtained, when the differences between the stations are lesser than 10%. Taking into account the work of Sicard et al. (2016), which provided DREff values of -122.0 ± 24.6 W m^{-2} τ^{-1} for a springtime mean aerosol in Palma de Mallorca (Spain; AOD^{440} = 0.51 and g^{440} = 0.70) over a period of 5 years, our study presents similar

305   results (< 10% lower). Obregón et al. (2015) studied two summer dust events over EVO and estimated DREff values of -112.9 ± 6.6 W m^{-2} τ^{-1} and -92.4 ± 9.8 W m^{-2} τ^{-1}, with a higher DREff reported for the first event attributed to the mixture of desert dust with smaller and more absorbing aerosols. However, the DREff at GRA of the present study are 1.5 times greater than those reported by Bazo et al. (2023) during an extreme dust event over GRA, but being similar with the DREff calculated by Granados-Muñoz et al. (2019).

310   **4.2.2 DRE at TOA and in the atmosphere**

The DRE at TOA is negative at each station during the entire dusty period, indicating a dust-induced cooling effect for all the stations considering in this study. Figure 5 shows the results at ARN station, for instance as an illustration in this work.

Similarly to results found at BOA, the first part of the dust outbreak (until 1 April) was moderate in terms of the radiative forcing (Córdoba-Jabonero et al., 2021) reaching DRE values induced by Df (Dc) particles above -10 W m^{-2} (-20 W m^{-2}).

315   During the rest of the episode, the dust event was weaker, with Df (Dc) DRE values above -5 W m^{-2} (-10 W m^{-2}). Finally, on 27 and 31 March (AOD ~ 0.80), Df (Dc) DRE reaches values above -40 W m^{-2} (-30 W m^{-2}) at ARN and -30 W m^{-2} (-20 Wm^{-2}) at TRJ. The maximum DRE values for the entire dust episode are found at ARN, reaching -35.9 W m^{-2} (-53.5 W m^{-2}) for Df (Dc) particles, with a DOD^{532} of 1.30.

Regarding the daily-averaged DRE over all the stations, with low and moderate DOD^{532} (< 0.5), reaches maximum values of

320   -10.8 W m^{-2} (-14.9 W m^{-2}) for Df (Dc) particles. In the case of high DOD^{532} (> 0.5), it reaches maximum values of -18.3 W m^{-2} (-21.4 W m^{-2}) for Df (Dc). The rest of the stations exhibit maximum values of approximately 35-70% lower than ARN. It

10

should be noted that the effect of the aerosol load is more pronounced for the Df than Dc particles, being DRE values 20% and 7% greater for high DOD^{532} (> 0.50) with respect low and medium DOD^{532} (< 0.50), respectively. The greatest episode-averaged DD DRE values are found at ARN, GRA and TRJ, ranging from -12.9 to -9.2 W m^{-2} and decreasing down to -6.7

325   and 6.0 W m^{-2} at EVO and BCN, respectively (see Table 5).

In comparison with other similar studies, results found in this work are in the upper range of DRE at TOA. Regarding the moderate dust event as described in Córdoba-Jabonero et al. (2021) at BCN as explained in the previous section (see Sect. 4.2.1), maximum DRE values of around -20 W m^{-2} (-25 W m^{-2}) as for Df (Dc) were reported. Moreover, in that work, the daily-averaged DRE varied from -1.7 to -6.1 W m^{-2} (from -2.0 to -9.5 W m^{-2}) for Df (Dc) particles during days with DOD^{532}

330   values ranging from 0.08 to 0.26. By comparing those results with the present study on BCN stations, for similar DODs, the dust outbreak shows similar daily DRE values for both Df and Dc particles. By considering the total dust contribution, Cachorro et al. (2008) reported values of -50.0 W m^{-2} during an intense dust episode over ARN. Moreover, Valenzuela et al. (2017) found daily DRE values that ranged from -19.2 to -35.1 W m^{-2} over EVO. In both cases, the present study shows daily DRE values 20%-30% lower than those reported.

335   Regarding the absolute evolution pattern of ftr_DRE (Table 5), from the linear regression analysis, the δDRE values range from 0.55 to 2.64 % day^{-1} for the different stations. That is, the contribution of Df particles to the total dust DRE presents a slight positive trend in each station during the dust outbreak, being this increase higher at TRJ than in others. It should be noted the case of GRA station, which shows negative values of almost 3 % day^{-1}. The episode-averaged ftr_DRE exhibits similar values of approximately 45% at all lidar stations (see Table 5), being a 5% higher than at BOA. Thus, the Df particles can induce almost half of the total dust DRE at TOA.

340   Similarly to the DRE at BOA, a linear regression analysis is performed to obtain DREff at both BOA and TOA values, computed for the five lidar stations, and for each dust component (Df, Dc, DD). Figure 6b-left and 6b-right shows, respectively, the linear fitting for ARN (taking as an example), and hence the DREff values obtained for all the stations. As for the BOA analysis, that linear fitting also shows a good degree of confidence with a correlation coefficient greater than 0.80 in each

345   station. By averaging those values for all the five stations, a mean DREff of -107.1 ± 10.4 $Wm^{-2}\tau^{-1}$ (-57.5 ± 3.3 $Wm^{-2}\tau^{-1}$) for Df (Dc) particles are found. In particular, for Dc particles, all the stations display very similar values, with the exception of TRJ, where are slightly higher. For Df particles, a higher variability is found (as indicated by the standard deviation of 10.4 W $m^{-2} \tau^{-1}$), ranging from a lower value found at GRA (-119.8 ± 7.6 W $m^{-2} \tau^{-1}$) to the higher one at TRJ (-92.7 ± 3.6 W $m^{-2} \tau^{-1}$). Thus, focusing in the separation of the component, Córdoba-Jabonero et al. (2021) observed DREff values of -98.6 ± 2.0 W

350    $m^{-2} \tau^{-1}$ (-43.9 ± 4.2 W $m^{-2} \tau^{-1}$) for Df (Dc) particles over BCN, i.e., values 9% (30%) lower than those found in the present study.

Regarding the DD component, an average value over the five lidar stations shows a DREff of -71.6 ± 4.2 W $m^{-2} \tau^{-1}$. In comparison with other similar works (as in Sect. 4.2.1), Sicard et al. (2016) observed a spring-averaged aerosol DD DREff of -83.4 ± 11.5 W $m^{-2} \tau^{-1}$ in Palma de Mallorca (Spain) over a period of 5 years, being values 16% greater. However, the DREff

11

355   at GRA of the present study are more than 3 times greater than those reported by Granados-Muñoz et al. (2019) for a dust
outbreak observed over GRA station.

The study of DREff allows assessing the radiative effect by eliminating the aerosol burden variable. However, not only is the
aerosol load significant of DRE calculations, but also the structure and altitude at which the dust is located. The most notable
difference among the studies from the literature presented here is the dust layering. In this work, the dust particles reached

360   several times the higher troposphere (over 6 km above sea level) over certain stations (TRJ and BCN). In those cases, the
plume is higher in the atmosphere. Thus, DRE is more pronounced and DREff is greater at DOD constant than a dust layer
located at lower altitudes.

Finally, results on the dust radiative effect in the atmospheric column are reported in Table 6. For instance, those values for
ARN station are shown in Figures 5a and 5b. By contrast with the DRE at BOA and TOA (see Sects. 3.3.1 and 3.3.2), the DRE

365   is positive for the entire episode, indicating an atmospheric dust-induced heating, as DRE(BOA) > DRE(TOA) in absolute
values (see Eq. 2). Regarding the episode average DRE, highest values are found at GRA, with +6.8 Wm^{-2} (+1.9 Wm^{-2}, +4.9
Wm^{-2}) for DD (Df, Dc) particles. Conversely, those values decrease with latitude, i.e. they are lower by 15% at ARN, 50% at
EVO, 25% at TRJ and 65% at BCN. The maximum DRE values are found at ARN, 83.5 W m^{-2} (22.9 W m^{-2}, 60.6 W m^{-2}) for
DD (Df, Dc) particles. For the rest of the stations the maxima DRE are lower, ranging from 55 % to 80 % with respect to those

370   found at ARN (see Table 6).

Similar results are found in terms of the atmospheric ftr_DRE ratio, showing approximately values in the 27-33% range.

4.3 Different approaches for DRE estimation in SW radiative flux simulations

As described in Sect. 2.2, a comparative analysis is performed by comparing the dust-induced DRE as obtained using two
different approaches. That is, by considering either the separated contributions of both dust modes (the novel approximation,

375   DRE$^{(I)}$) or the contribution of the total dust in overall (the commonly used, DRE$^{(II)}$). Note that the second approach (DRE$^{(II)}$),
which is widely used by other authors, will be taken as the reference value in the comparison (see Eq. 6).

Thus g is a key parameter in radiative transfer calculation, Figure 7 shows the dependence of ΔDRE with respect to g^{440} at
both BOA and TOA, for all the five lidar stations considered in this study. In addition, those corresponding values are colour-
highlighted depending on the SZA, DOD^{532} and the difference between the fine and total g^{440} values; i.e., $\Delta g^{440} =$

380    $fine\ g^{440} - total\ g^{440}$.

Since GAME uses a plane-parallel atmosphere approximation (see Sect. 2.1), it is likely that large errors are obtained by
calculating DRE at SZA > 70º. Hence, higher differences in ΔDRE could be observed (Fig. 7a-7b, left). Moreover, the ΔDRE
are generally larger as the DOD^{532} increases (Fig. 7a-7b center), generally for DOD^{532} > 0.50. Conclusions regarding the Df/DD
ratio of the DOD^{532} cannot be drawn, as the relative fraction of Df and Dc particles remained approximately constant in altitude

385   at each station along the overall dust episode (i.e., Df and Dc particles were well-mixed along the atmospheric column; see
Sect. 3). Indeed, the Df/DD ratio of the DOD^{532} was around 30% (López-Cayuela et al., 2023). Regarding this result, and due
to DRE exhibits a strong dependency on DOD, ΔDRE is generally greater when DRE$^{(II)}$ increases (see Fig. S10 in the

Supplementary Material). Particularly, ΔDRE increases for $DRE^{(II)}$ values greater than 40 and 30 W m^{-2} at BOA and TOA, respectively.

390 Furthermore, 80% of the all-hourly DRE under study does not exceed a threshold of $\pm15\%$ in their relative differences. Indeed, considering $g^{440} \leq 0.73$, ΔDRE are not significant, showing mean (relative) differences of -0.6 W m^{-2} (-10%) for both BOA and TOA. However, greater negative differences are observed for $g^{440} > 0.73$ (for almost purely forward-scattering particles). Indeed, the dispersion increases significantly, reaching maximum ΔDRE values of approximately -20 W m^{-2}. A priori, this result may appear surprising since a dust outbreak is dominated by coarse particles. However, what sets the difference apart is

395 the proportion of the fine particles of the intrusion. Regarding the values of Δg^{440} (Figure 7a-7b, right), it seems that the ΔDRE values are greater for $\Delta g^{440} > 0.1$. Thus, the fine particles seem to play a key role in radiative transfer computations. To summarize, ΔDRE are quite similar at both TOA and BOA. Approximately 60% (40%) of ΔDRE exhibits positive (negative) values. That means that, applying the separation of the dust modes, at both TOA and BOA around 60% (40%) of the DRE values are overestimated (underestimated) in a mean value of 9% (13%) in terms of the relative differences. A precise

400 estimation of g holds to the potential to significantly enhance the assessment of the aerosol radiative effect, and one of the main differences between the two approaches used in this study is the value of g considered. Regarding other authors, Andrews et al. (2006) determined that a 10% decrease in g would correspond to a 13 and 19 % reduction in BOA and TOA forcing, respectively. These findings align with those observed in our study. It is expected to yield $DRE^{(I)}$ results that over-/underestimate $DRE^{(II)}$ values at certain degree.

405 **5. Summary and conclusions**

This article serves as a complement to the study conducted by López-Cayuela et al. (2023), about an intense dust episode that took place between 25 March and 7 April 2021 over the Iberian Peninsula. This study focuses on the estimation of temporal variations in the instantaneous and daily direct radiative effects of dust in the short-wave spectral range. The investigation is carried out using data obtained from five lidar stations situated in El Arenosillo/Huelva, Granada, Torrejón/Madrid and

410 Barcelona in Spain, as well as Évora in Portugal. The vertical distribution of both the fine- and coarse-mode dust is derived from López-Cayuela et al. (2023). The main findings are summarised next.
Across all the stations examined in this study, the DRE remains negative throughout the dusty period at both BOA and TOA, indicating aerosol-induced cooling at these levels. Conversely, within the atmosphere, the DRE shows a positive trend, indicating aerosol-induced heating. The results are similar with those reported by a wide range of studies that can be found in

415 the literature. In some specific days, the DRE results were considerably high, corresponding to DODs greater than 0.80. Particularly, this work shows maximum hourly averaged values of -54.1 W m^{-2} (-96.3 W m^{-2}) and -35.9 W m^{-2} (-53.5 W m^{-2}) for Df (Dc) particles at BOA and TOA, respectively. It is important to emphasize that, despite dust intrusions are primarily governed by the coarse dust mode, the contribution of the fine dust mode should not be systematically disregarded in radiative

transfer simulations. In this particular dust outbreak (with an episode-average ftr_DOD of 30% for all the stations considered

420 in this study), the Df particles produced almost half of the total DRE at both BOA and TOA.

In terms of DREff, similar values are found at every station, with variation lesser than 10% between them. By comparing with other authors, this study shows DREff values slightly higher for Df particles (< 10%) at both BOA and TOA. However, the difference increases for Dc particles, with DREff values being a 15% greater at BOA and 30% higher at TOA than those reported by other works. In terms of DD particles, the DREff results are similar to those reported at BOA, and higher at TOA.

425 It can be concluded that separating both dust components may lead to an overestimation of the DRE. In this study, the effect is more pronounced at the TOA than at the BOA, probably due to the presence of dust at higher levels than those usual in the troposphere. This fact can introduce relevant implications for radiometric measurements from satellite instrumentation.

Finally, differences were found by simulating DRE using the two different approaches. Separating both Df and Dc components implies that 60% (40%) of the DRE values are overestimated (underestimated) in comparison with the classical approach. In

430 particular, relative differences of 9% overestimation and 13% underestimation in average were found at both TOA and BOA. However, it is important to highlight the differences are not significant in 80% of all hourly data, not exceeding a threshold of ±15% in terms of the relative differences in DRE. The greater differences in DRE between both methodologies, which reached values of -20 W m^{-2}, are likely related to the role of Df particles. In particular, they are likely related to using in the radiative transfer model the asymmetry factor of both components separately, in dependence of the proximity of the asymmetry factor

435 of the fine particles to that of the total dust.

For future work, it would be relevant to perform the same study, but under dusty conditions with rather variable ftr_DOD, to comprehensively assess the role of the fine particles in DRE by using two different conceptual approaches. This would allow determining how dust aging affects the DRE, as considered looking at the proportion of Df particles relative to DD.

Data availability

440 EARLINET lidar files are available from the EARLINET Data Portal (https://data.earlinet.org/, last access: 21 December 2021; Pappalardo et al., 2014). The accessibility of these files is limited based on the EARLINET criteria. Part of the data used in this publication was obtained as part of the AERONET network and is publicly available. For additional lidar data or information, please contact the corresponding author.

Author contributions

445 CCJ and JLGR conceptualized the study. MÁLC, CCJ, MS and JLGR were responsible for the formal analysis. MÁLC wrote the original draft of the paper and applied the software. MÁLC, CCJ, MS, and JLGR carried out the investigation. MÁLC, CCJ, MS, VS, MJGM, AC, FTC, JABA, CMP, MJC, ARG, DB, JAG, LAA and JLGR reviewed and edited the paper. CCJ,

14

MJGM, ARG and DB were responsible for data curation. CCJ, LAA, AC and MJC provided the resources. CCJ and JLGR supervised the investigation. All authors have read and agreed upon the published version of the paper.

Competing interests

The contact author has declared that none of the authors has any competing interests.

References

Allen, R. J., Landuyt, W., and Rumbold, S. T.: An increase in aerosol burden and radiative effects in a warmer world, Nat. Clim. Change, 6, 269–274, doi:10.1038/nclimate2827, 2016.

Andrews, E., Sheridan, P.J., Fiebig, M., McComiskey, A., Ogren, J. A., Arnott, P., Covert, D., Elleman, R., Gasparini, R., Collins, D., Jonsson, H., Scchmid, B., and Wang, J.: Comparison of methods for deriving aerosol asymmetry parameters, J. Geophys. Res., 111, D05S04, doi:10.1029/2004jd005734, 2006.

Ansmann, A., Mamouri, R.-E., Hofer, J., Baars, H., Althausen, D., and Abdullaev, S. F.: Dust mass, cloud condensation nuclei, and ice-nucleating particle profiling with polarization lidar: updated POLIPHON conversion factors from global AERONET analysis, Atmospheric Meas. Tech., 12, 4849–4865, doi:10.5194/amt-12-4849-2019, 2019.

Arias, P., Bellouin, N., Coppola, E., Jones, R., Krinner, G., Marotzke, J., Naik, V., Palmer, M., Plattner, G.-K., Rogelj, J., Rojas, M., Sillmann, J., Storelvmo, T., Thorne, P., Trewin, B., Achutarao, K., Adhikary, B., Allan, R., Armour, K., Bala, G.,

Barimalala, R., Berger, S., Canadell, J. G., Cassou, C., Cherchi, A., Collins, W. D., Collins, W. J., Connors, S., Corti, S., Cruz, F., Dentener, F. J., Dereczynski, C., Di Luca, A., Diongue Niang, A., Doblas-Reyes, P., Dosio, A., Douville, H., Engelbrecht, F., Eyring, V., Fischer, E. M., Forster, P., Fox-Kemper, B., Fuglestvedt, J., Fyfe, J., Gillett, N., Goldfarb, L., Gorodetskaya, I., Gutierrez, J. M., Hamdi, R., Hawkins, E., Hewitt, H., Hope, P., Islam, A. S., Jones, C., Kaufmann, D., Kopp, R., Kosaka, Y.,

480   Kossin, J., Krakovska, S., Li, J., Lee, J.-Y., Masson-Delmotte, V., Mauritsen, T., Maycock, T., Meinshausen, M., Min, S., Ngo Duc, T., Otto, F., Pinto, I., Pirani, A., Raghavan, K., Ranasighe, R., Ruane, A., Ruiz, L., Sallée, J.-B., Samset, B. H., Sathyendranath, S., Monteiro, P. S., Seneviratne, S. I., Sörensson, A. A., Szopa, S., Takayabu, I., Treguier, A.-M., van den Hurk, B., Vautard, R., Von Schuckmann, K., Zaehle, S., Zhang, X., and Zickfeld, K.: Climate Change 2021: The Physical Science Basis. Contribution of Working Group I to the Sixth Assessment Report of the Intergovernmental Panel on Climate

485   Change; Technical Summary, The Intergovernmental Panel on Climate Change AR6, Remote, 2021.

Barragan, R., Romano, S., Sicard, M., Burlizzi, P., Perrone, M. R., and Comeron, A.: Estimation of mineral dust direct radiative forcing at the European Aerosol Research Lidar NETwork site of Lecce, Italy, during the ChArMEx/ADRIMED summer 2013 campaign: Impact of radiative transfer model spectral resolutions, J. Geophys. Res. Atmospheres, 121, 10,237-10, 261, doi:10.1002/2016JD025016, 2016.

490   Bazo, E., Granados-Muñoz, M. J., Román, R., Bravo-Aranda, J. A., Cazorla, A., Valenzuela, A., González, R., Olmo, F. J., and Alados-Arboledas, L.: Evaluation of the vertically-resolved aerosol radiative effect on shortwave and longwave ranges using sun-sky photometer and ceilometer measurements, Atmospheric Res., 282, 106517, doi:10.1016/j.atmosres.2022.106517, 2023.

Cachorro, V. E., Toledano, C., Prats, N., Sorribas, M., Mogo, S., Berjón, A., Torres, B., Rodrigo, R., Rosa, J. de la, and Frutos,

495   A. M. D.: The strongest desert dust intrusion mixed with smoke over the Iberian Peninsula registered with Sun photometry, J. Geophys. Res. Atmospheres, 113, doi:10.1029/2007JD009582, 2008.

Cazorla, A., Casquero-Vera, J. A., Román, R., Guerrero-Rascado, J. L., Toledano, C., Cachorro, V. E., Orza, J. A. G., Cancillo, M. L., Serrano, A., Titos, G., Pandolfi, M., Alastuey, A., Hanrieder, N., and Alados-Arboledas, L.: Near-real-time processing of a ceilometer network assisted with sun-photometer data: monitoring a dust outbreak over the Iberian Peninsula, Atmospheric

500   Chem. Phys., 17, 11861–11876, doi:10.5194/acp-17-11861-2017, 2017.

Córdoba-Jabonero, C., Sicard, M., Ansmann, A., Águila, A. del, and Baars, H.: Vertical separation of the atmospheric aerosol components by using poliphon retrieval in polarized micro pulse lidar (P-MPL) measurements: case studies of specific climate-relevant aerosol types, EPJ Web Conf., 176, 05041, doi:10.1051/epjconf/201817605041, 2018.

Córdoba-Jabonero, C., Sicard, M., del Águila, A., Jiménez, M., and Zorzano, M.-P.: Performance of a dust model to predict

505   the vertical mass concentration of an extreme Saharan dust event in the Iberian Peninsula: Comparison with continuous, elastic, polarization-sensitive lidars, Atmos. Environ., 214, 116828, doi:10.1016/j.atmosenv.2019.116828, 2019.

Córdoba-Jabonero, C., Sicard, M., López-Cayuela, M.-Á., Ansmann, A., Comerón, A., Zorzano, M.-P., Rodríguez-Gómez, A., and Muñoz-Pocar, C.: Aerosol radiative effect during the summer 2019 heatwave produced partly by an inter-continental

16

Saharan dust outbreak. 1. Shortwave dust-induced direct impact, Atmospheric Chem. Phys., 21, 6455–6479, doi:10.5194/acp-
510   2020-1013, 2021.

Couto, F.T., Cardoso, E., Costa, M. J., Salgado, R., Guerrero-Rascado, J. L., Salgueiro, V.: How a mesoscale cyclonic vortex over Sahara leads to a dust outbreak in South-western Iberia, Atmos, Res., 249, 105302, doi:10.1016/j.atmosres.2020.105302, 2021.

Dubovik, O., Smirnov, A., Holben, B. N., King, M. D., Kaufman, Y. J., Eck, T. F., and Slutsker, I.: Accuracy assessments of
515   aerosol optical properties retrieved from Aerosol Robotic Network (AERONET) Sun and sky radiance measurements, J. Geophys. Res. Atmospheres, 105, 9791–9806, doi:10.1029/2000JD900040, 2000.

Dubovik, O., Holben, B., Eck, T. F., Smirnov, A., Kaufman, Y. J., King, M. D., Tanré, D., and Slutsker, I.: Variability of absorption and optical properties of key aerosol types observed in worldwide locations, J. Atmospheric Sci., 59, 590–608, doi:10.1175/1520-0469(2002)059<0590:VOAAOP>2.0.CO;2, 2002.

520   Dubuisson, P., Buriez, J. C., and Fouquart, Y.: High spectral resolution solar radiative transfer in absorbing and scattering media: Application to the satellite simulation, J. Quant. Spectrosc. Radiat. Transf., 55, 103–126, doi:10.1016/0022-4073(95)00134-4, 1996.

Dubuisson, P., Dessailly, D., Vesperini, M., and Frouin, R.: Water vapor retrieval over ocean using near-infrared radiometry, J. Geophys. Res. Atmospheres, 109, doi:10.1029/2004JD004516, 2004.

525   Fernández, A. J., Sicard, M., Costa, M. J., Guerrero-Rascado, J. L., Gómez-Amo, J. L., Molero, F., Barragán, R., Basart, S., Bortoli, D., Bedoya-Velásquez, A. E., Utrillas, M. P., Salvador, P., Granados-Muñoz, M. J., Potes, M., Ortiz-Amezcua, P., Martínez-Lozano, J. A., Artíñano, B., Muñoz-Porcar, C., Salgado, R., Román, R., Rocadenbosch, F., Salgueiro, V., Benavent-Oltra, J. A., Rodríguez-Gómez, A., Alados-Arboledas, L., Comerón, A., and Pujadas, M.: Extreme, wintertime Saharan dust intrusion in the Iberian Peninsula: Lidar monitoring and evaluation of dust forecast models during the February 2017 event,
530   Atmospheric Res., 228, 223–241, doi:10.1016/j.atmosres.2019.06.007, 2019.

Granados-Muñoz, M. J., Sicard, M., Román, R., Benavent-Oltra, J. A., Barragan, R., Brogniez, G., Denjean, C., Mallet, M., Formenti, P., Torres, B., and Alados-Arboledas, L.: Impact of mineral dust on shortwave and longwave radiation: evaluation of different vertically resolved parameterizations in 1-D radiative transfer computations, Atmospheric Chem. Phys., 19, 523–542, doi:10.5194/acp-19-523-2019, 2019.

535   Guerrero-Rascado, J. L., Olmo, F. J., Avilés-Rodríguez, I., Navas-Guzmán, F., Pérez-Ramírez, D., Lyamani, H., and Alados Arboledas, L.: Extreme Saharan dust event over the southern Iberian Peninsula in september 2007: active and passive remote sensing from surface and satellite, Atmospheric Chem. Phys., 9, 8453–8469, doi:10.5194/acp-9-8453-2009, 2009.

Kok, J. F., Ward, D. S., Mahowald, N. M., and Evan, A. T.: Global and regional importance of the direct dust-climate feedback, Nat. Commun., 9, 241, doi:10.1038/s41467-017-02620-y, 2018.

540   Kok, J. F., Adebiyi, A. A., Albani, S., Balkanski, Y., Checa-Garcia, R., Chin, M., Colarco, P. R., Hamilton, D. S., Huang, Y., Ito, A., Klose, M., Li, L., Mahowald, N. M., Miller, R. L., Obiso, V., Pérez García-Pando, C., Rocha-Lima, A., and Wan, J.

S.: Contribution of the world's main dust source regions to the global cycle of desert dust, Atmospheric Chem. Phys., 21, 8169–8193, doi:10.5194/acp-21-8169-2021, 2021.

545 Kok, J. F., Storelvmo, T., Karydis, V. A., Adebiyi, A. A., Mahowald, N. M., Evan, A. T., He, C., and Leung, D. M.: Mineral dust aerosol impacts on global climate and climate change, Nat. Rev. Earth Environ., 4, 71–86, doi:10.1038/s43017-022-00379-5, 2023.

Lacis, A. A. and Oinas, V.: A description of the correlated k distribution method for modeling nongray gaseous absorption, thermal emission, and multiple scattering in vertically inhomogeneous atmospheres, J. Geophys. Res. Atmospheres, 96, 9027–9063, doi:10.1029/90JD01945, 1991.

550 Lolli, S., Madonna, F., Rosoldi, M., Campbell, J. R., Welton, E. J., Lewis, J. R., Gu, Y., and Pappalardo, G.: Impact of varying lidar measurement and data processing techniques in evaluating cirrus cloud and aerosol direct radiative effects, Atmospheric Meas. Tech., 11, 1639–1651, doi:10.5194/amt-11-1639-2018, 2018.

López-Cayuela, M. Á., Córdoba-Jabonero, C., Bermejo-Pantaleón, D., Sicard, M., Salgueiro, V., Molero, F., Carvajal-Pérez, C. V., Granados-Muñoz, M. J., Comerón, A., Couto, F. T., Barragán, R., Zorzano, M.-P., Bravo-Aranda, J. A., Muñoz-Porcar,

555 C., Costa, M. J., Artíñano, B., Rodríguez-Gómez, A., Bortoli, D., Pujadas, M., Abril-Gago, J., Alados-Arboledas, L., and Guerrero-Rascado, J. L.: Vertical characterization of fine and coarse dust particles during an intense Saharan dust outbreak over the Iberian Peninsula in springtime 2021, Atmospheric Chem. Phys., 23, 143–161, doi:10.5194/acp-23-143-2023, 2023.

Mamouri, R. E. and Ansmann, A.: Fine and coarse dust separation with polarization lidar, Atmospheric Meas. Tech., 7, 3717–3735, doi:10.5194/amt-7-3717-2014, 2014.

560 Mamouri, R.-E. and Ansmann, A.: Potential of polarization/Raman lidar to separate fine dust, coarse dust, maritime, and anthropogenic aerosol profiles, Atmospheric Meas. Tech., 10, 3403–3427, doi:10.5194/amt-10-3403-2017, 2017.

Meloni, D., di Sarra, A., Di Iorio, T., and Fiocco, G.: Influence of the vertical profile of Saharan dust on the visible direct radiative forcing, J. Quant. Spectrosc. Radiat. Transf., 93, 397–413, doi:10.1016/j.jqsrt.2004.08.035, 2005.

Meloni, D., di Sarra, A., Brogniez, G., Denjean, C., De Silvestri, L., Di Iorio, T., Formenti, P., Gómez-Amo, J. L., Gröbner,

565 J., Kouremeti, N., Liuzzi, G., Mallet, M., Pace, G., and Sferlazzo, D. M.: Determining the infrared radiative effects of Saharan dust: a radiative transfer modelling study based on vertically resolved measurements at Lampedusa, Atmospheric Chem. Phys., 18, 4377–4401, doi:10.5194/acp-18-4377-2018, 2018.

Obregón, M. A., Pereira, S., Salgueiro, V., Costa, M. J., Silva, A. M., Serrano, A., Bortoli, D.: Aerosol radiative effects during two desert dust events in August 2012 over the southwestern Iberian Peninsula, Atmos. Res., 153, 404-415,

570 doi:10.1016/j.atmosres.2014.10.007, 2015.

Prasad, A. K., Singh, S., Chauhan, S. S., Srivastava, M. K., Singh, R. P., and Singh, R.: Aerosol radiative forcing over the Indo-Gangetic plains during major dust storms, Atmos. Environ., 41, 6289–6301, doi:10.1016/j.atmosenv.2007.03.060, 2007.

Preißler, J., Wagner, F., Pereira, S. N., and Guerrero-Rascado, J. L.: Multi-instrumental observation of an exceptionally strong Saharan dust outbreak over Portugal, J. Geophys. Res. Atmospheres, 116, doi:10.1029/2011JD016527, 2011.

575   Russo, A., Sousa, P. M., Durão, R. M., Ramos, A. M., Salvador, P., Linares, C., Díaz, J., and Trigo, R. M.: Saharan dust intrusions in the Iberian Peninsula: Predominant synoptic conditions, Sci. Total Environ., 717, 137041, doi:10.1016/j.scitotenv.2020.137041, 2020.

Salvador, P., Pey, J., Pérez, N., Querol, X., and Artíñano, B.: Increasing atmospheric dust transport towards the western Mediterranean over 1948–2020, Npj Clim. Atmospheric Sci., 5, 1–10, doi:10.1038/s41612-022-00256-4, 2022.

580   Santos, D., Costa, M. J., Silva, A. M., Guerrero-Rascado, J. L.: Modeling Saharan desert dust radiative effects on clouds, Atmos. Res., 127, doi:10.1016/j.atmosres.2012.09.024, 2013.

Sicard, M., Bertolín, S., Mallet, M., Dubuisson, P., and Comerón, A.: Estimation of mineral dust long-wave radiative forcing: sensitivity study to particle properties and application to real cases in the region of Barcelona, Atmospheric Chem. Phys., 14, 9213–9231, doi:10.5194/acp-14-9213-2014, 2014a.

585   Sicard, M., Bertolín, S., Muñoz, C., Rodríguez, A., Rocadenbosch, F., and Comerón, A.: Separation of aerosol fine- and coarse-mode radiative properties: Effect on the mineral dust longwave, direct radiative forcing, Geophys. Res. Lett., 41, 6978–6985, doi:10.1002/2014GL060946, 2014b.

Sicard, M., Barragan, R., Dulac, F., Alados-Arboledas, L., and Mallet, M.: Aerosol optical, microphysical and radiative properties at regional background insular sites in the western Mediterranean, Atmospheric Chem. Phys., 16, 12177–12203,

590   doi:10.5194/acp-16-12177-2016, 2016.

Sicard, M., Córdoba-Jabonero, C., López-Cayuela, M.-Á., Ansmann, A., Comerón, A., Zorzano, M.-P., Rodríguez-Gómez, A., and Muñoz-Porcar, C.: Aerosol radiative impact during the summer 2019 heatwave produced partly by an inter-continental Saharan dust outbreak – Part 2: Long-wave and net dust direct radiative effect, Atmospheric Chem. Phys., 22, 1921–1937, doi:10.5194/acp-22-1921-2022, 2022.

595   Sorribas, M., Adame, J. A., Andrews, E., and Yela, M.: An anomalous African dust event and its impact on aerosol radiative forcing on the Southwest Atlantic coast of Europe in February 2016, Sci. Total Environ., 583, 269–279, doi:10.1016/j.scitotenv.2017.01.064, 2017.

Sousa, P. M., Barriopedro, D., Ramos, A. M., García-Herrera, R., Espírito-Santo, F., and Trigo, R. M.: Saharan air intrusions as a relevant mechanism for Iberian heatwaves: The record breaking events of August 2018 and June 2019, Weather Clim.

600   Extrem., 26, 100224, doi:10.1016/j.wace.2019.100224, 2019.

Stamnes, K., Tsay, S.-C., Wiscombe, W., and Jayaweera, K.: Numerically stable algorithm for discrete-ordinate-method radiative transfer in multiple scattering and emitting layered media, Appl. Opt., 27, 2502, doi:10.1364/AO.27.002502, 1988.

Tegen, I. and Schepanski, K.: Climate Feedback on Aerosol Emission and Atmospheric Concentrations, Curr. Clim. Change Rep., 4, 1–10, doi:10.1007/s40641-018-0086-1, 2018.

605   Titos, G., Ealo, M., Pandolfi, M., Pérez, N., Sola, Y., Sicard, M., Comerón, A., Querol, X., and Alastuey, A.: Spatiotemporal evolution of a severe winter dust event in the western Mediterranean: Aerosol optical and physical properties, J. Geophys. Res. Atmospheres, 122, 4052–4069, doi:10.1002/2016JD026252, 2017.

Valenzuela, A., Costa, M. J., Guerrero-Rascado, J. L., Bortoli, D., and Olmo, F. J.: Solar and thermal radiative effects during the 2011 extreme desert dust episode over Portugal, Atmos. Environ., 148, 16–29, doi:10.1016/j.atmosenv.2016.10.037, 2017.
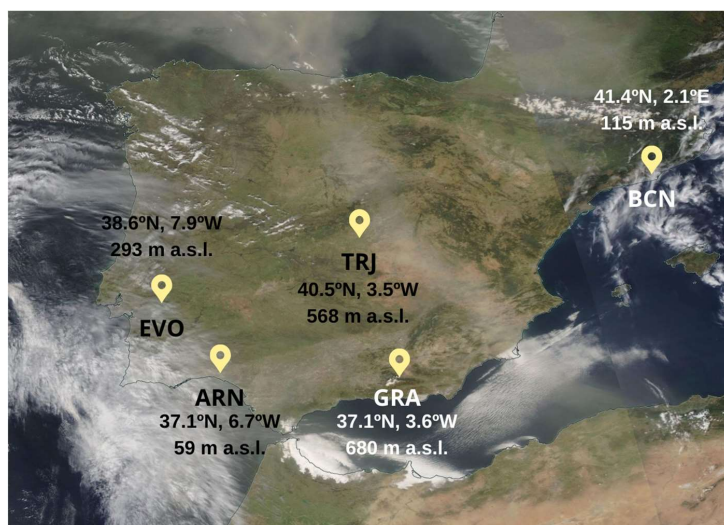
610

Figure 1: MODIS Terra/Aqua corrected reflectance over the Iberian Peninsula on 31 March 2021. The five lidar stations are marked with a yellow pin. From south-west to north-east: El Arenosillo/Huelva (ARN), Évora (EVO), Granada (GRA), Torrejón/Madrid (TRJ) and Barcelona (BCN) sites. The coordinates and altitude are also included.
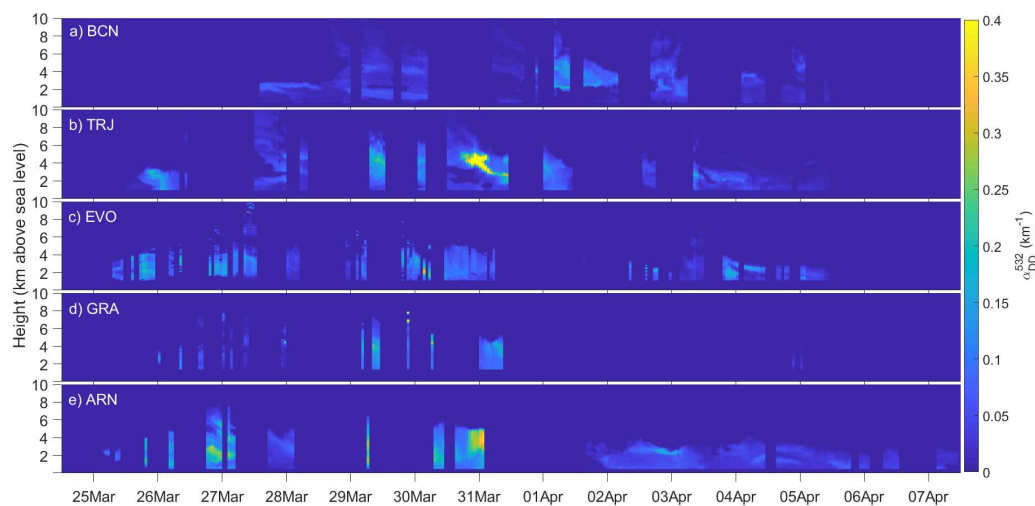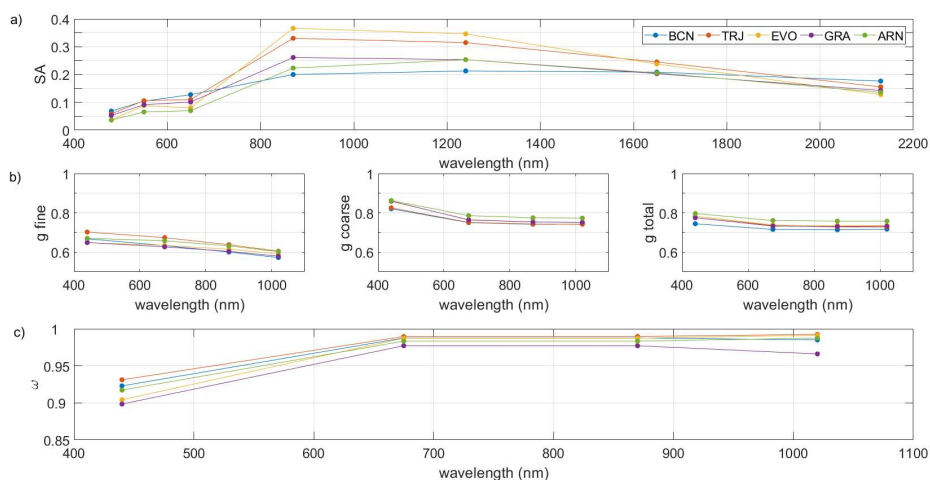
615

Figure 2: Temporal evolution of the DD extinction coefficient (α_{DD}^{532}, km⁻¹) at the five Iberian lidar stations (from North-East to South-West IP, by decreasing latitude): a) Barcelona (BCN), b) Torrejón/Madrid (TRJ), c) Évora (EVO), d) Granada (GRA) and e) El Arenosillo/Huelva (ARN). Profile gaps correspond to impossibility of inversion or no lidar measurements.

620

Figure 3: Spectral behaviour of (a) the mean of the MODIS surface albedo (SA) distribution, (b) AERONET asymmetry factor (g) for fine, coarse and total modes, and (c) AERONET single scattering albedo (ω) at the five Iberian lidar stations: Barcelona (BCN, blue), Torrejón/Madrid (TRJ, orange), Évora (EVO, yellow), Granada (GRA, purple) and El Arenosillo/Huelva (ARN, green). The date and time chosen is 1 April at 10 UTC for BCN station and 31 March at 12 UTC for the rest of the sites.
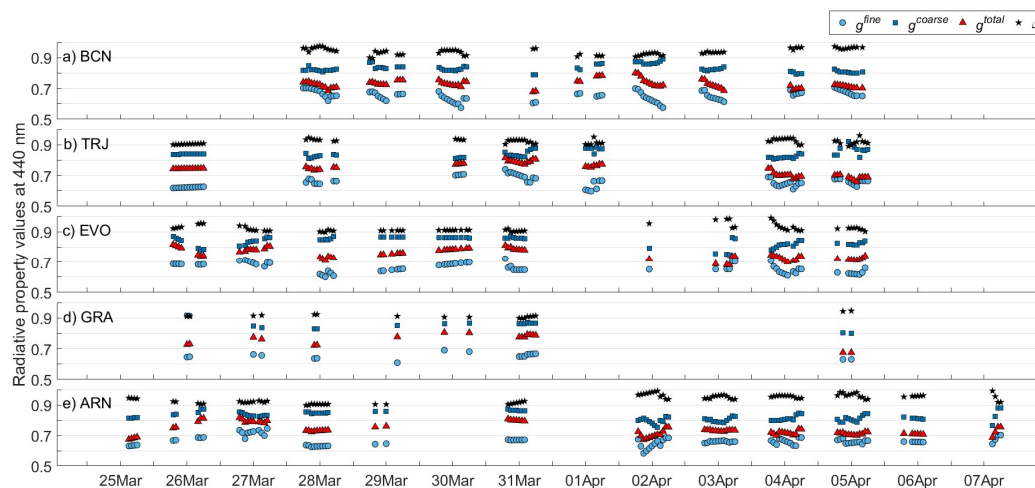
Figure 4: Overview of the temporal evolution of the radiative properties of fine, coarse and total g, and for ω at 440 nm at the five lidar stations, i.e., (a) BCN, (b) TRJ, (c) EVO, (d) GRA and (e) ARN.
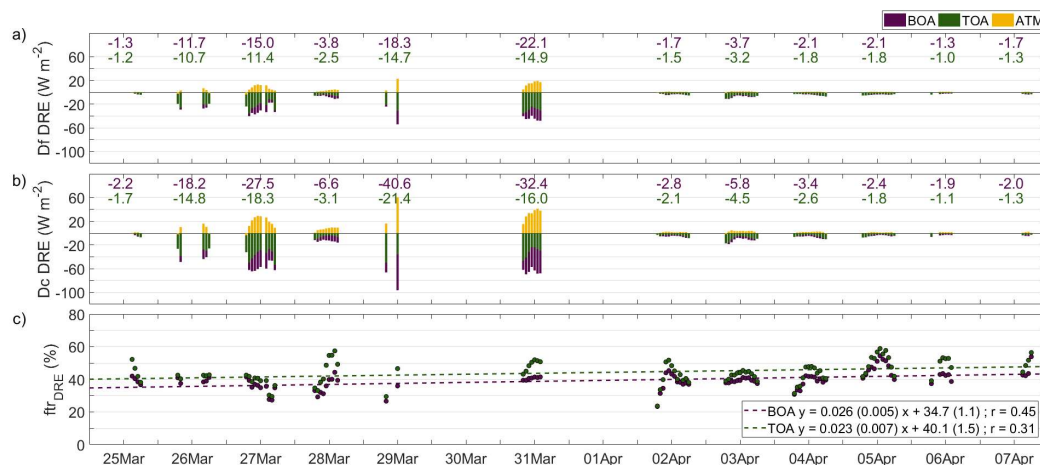
Figure 5: Dust direct radiative effect (DRE, W m^{-2}) at BOA (purple), TOA (green) and in the atmosphere (ATM, yellow) at the ARN station as induced by the (a) fine dust (Df) and (b) coarse dust particles. Daily mean values are also included above (keeping the same colours). (c) Fine-to-total (Df/DD) ratio of the dust DRE (ftr_DRE) at BOA (purple) and TOA (green), together with their linear fit between 25 March and 7 April. The standard deviation of the slope and intercept are shown in brackets. The absolute temporal rate of the ftr_DRE ratio (δDRE) at BOA (TOA) is +0.026% h^{-1} (+0.023 % h^{-1}), being equivalent to an increase of +0.62 % day^{-1} (+0.55 % day^{-1}).

635
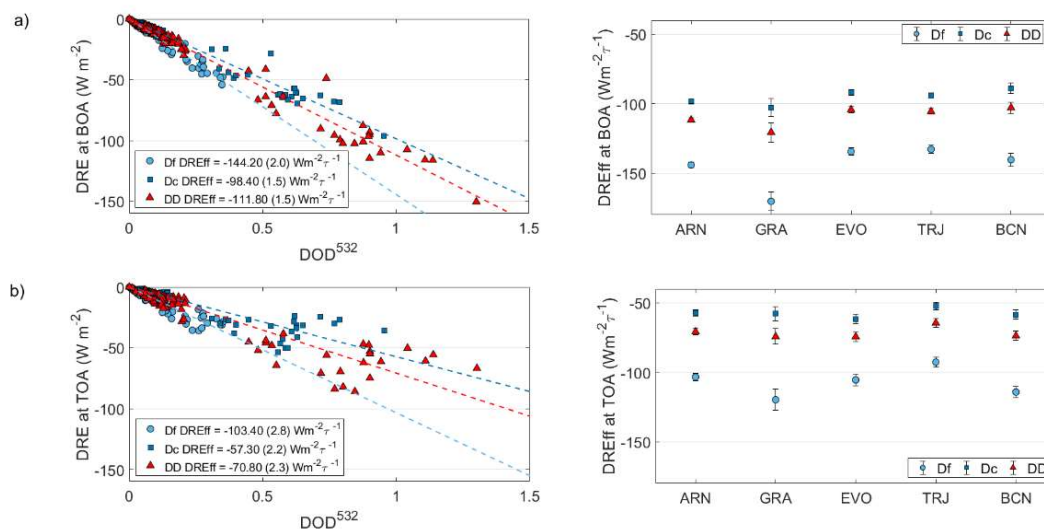
Figure 6: Dust direct radiative effect (DRE) as a function of DOD^{532} for instance at ARN station (left panels), together with the DREff values as obtained for each station (right panels), at a) BOA, and b) TOA. Both are shown separately for the fine dust (Df, blue circles), coarse dust (Dc, dark blue squares) and total dust (DD, red triangles). The error of the DREff are shown in brackets in the left panels, and by bars in the right panels. The period consider is from 25 March to 7 April 2021.

640
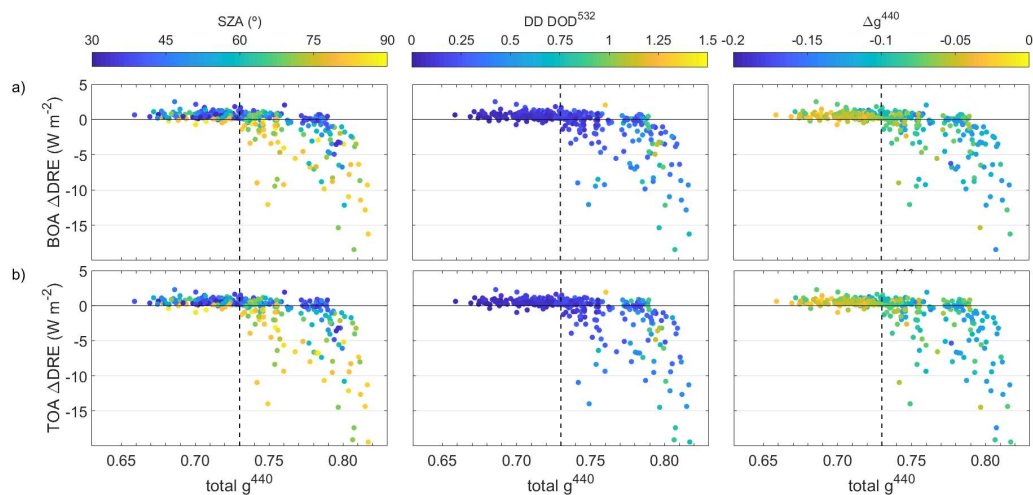
Figure 7: Differences in DRE (ΔDRE; W m⁻²) as obtained between the two approaches with respect to total g^{440} at a) BOA and b) TOA for all the five lidar stations involved in this study from 25 March to 7 April 2021. The dependence on the solar zenith angle (SZA, °), DD DOD^{532} and Δg is shown by a colour-scaled bar. The dashed line marks the threshold of $g = 0.73$.

Table 1: Input parameters and radiative properties for the GAME model and databases in the SW spectral range. Note that z denotes the vertical dependence.

	Parameters	Database / instrumentation
Atmosphere and Land	SA	MODIS
	Atmospheric profiles	U.S. std. atm. + 3h GDAS profiles
	Gas concentration profiles	U.S. std. atm. + 3h GDAS profiles
	Absorption coefficients	HITRAN
Aerosols	$\alpha^{532}(z)$ (fine, coarse, DD)	Lidar
	DOD (fine, coarse, DD)	Lidar + Sun-photometer
	g (fine, coarse, total)	Sun-photometer
	ω (total)	Sun-photometer
	$AE^{440-870}$	Sun-photometer

Table 2: Dust optical depth at 532 nm (DOD[532]) for the dust fine (Df) and coarse (Dc) components and DD (DD = Df + Dc) at the five lidar stations (from left to right as latitude increases). ftr_DOD denotes the Df-to-DD ratio (in %). $\overline{X}$ indicates the average for the whole dust event (the standard deviation is also shown) and X^{max} refers to the maximal hourly value within the dusty period.

	ARN	GRA	EVO	TRJ	BCN
$\overline{Df}$	0.10 ± 0.10	0.08 ± 0.06	0.06 ± 0.03	0.08 ± 0.07	0.04 ± 0.02
$\overline{Dc}$	0.24 ± 0.25	0.20 ± 0.16	0.15 ± 0.08	0.19 ± 0.15	0.10 ± 0.06
$\overline{DD}$	0.34 ± 0.35	0.28 ± 0.22	0.21 ± 0.11	0.27 ± 0.22	0.14 ± 0.08
ftr_DOD (%)	29.4	28.6	30.0	28.5	28.6
Df^{max}	0.35	0.18	0.19	0.27	0.16
Dc^{max}	0.95	0.49	0.42	0.61	0.38
DD^{max}	1.30	0.65	0.61	0.88	0.54

Table 3: Radiative properties at 440 nm at the five lidar stations (from left to right as latitude increases). Particularly, the parameters are: the dust fine (Df) and coarse (Dc) components of the asymmetry factor (g); and the total dust component for both g and single scattering albedo (ω). The symbol $\overline{X}$ indicates the average for the whole dust event (the standard deviation is also shown) and X^{max} and X^{min} refers to the maximal and minimal hourly value within the dusty period, respectively.

		ARN	GRA	EVO	TRJ	BCN
	$\overline{Df}$	0.662 ± 0.029	0.652 ± 0.020	0.661 ± 0.031	0.658 ± 0.033	0.652 ± 0.032
	Df^{max}	0.746	0.691	0.722	0.740	0.706
	Df^{min}	0.575	0.599	0.601	0.599	0.575
	$\overline{Dc}$	0.822 ± 0.028	0.856 ± 0.030	0.837 ± 0.031	0.841 ± 0.025	0.829 ± 0.024
g^{440}	Dc^{max}	0.881	0.917	0.870	0.920	0.892
	Df^{min}	0.755	0.798	0.750	0.807	0.788
	$\overline{total\ dust}$	0.735 ± 0.037	0.759 ± 0.041	0.754 ± 0.035	0.740 ± 0.038	0.728 ± 0.026
	$total\ dust^{max}$	0.817	0.805	0.816	0.815	0.800
	$total\ dust^{min}$	0.672	0.675	0.681	0.659	0.678
	$\overline{total\ dust}$	0.941 ± 0.026	0.914 ± 0.013	0.922 ± 0.022	0.921 ± 0.016	0.941 ± 0.021
ω^{440}	$total\ dust^{max}$	0.992	0.946	0.990	0.960	0.976
	$total\ dust^{min}$	0.897	0.898	0.897	0.890	0.897

655

660

665

670 **Table 4: Episode-averaged hourly values of the dust radiative effect (DRE, in W m^{-2}) and their standard deviation on the surface (BOA) as induced by fine (Dc), coarse (Dc) and total dust (DD) at the five Iberian lidar stations. $\overline{X}$ indicates the average for the whole event (standard deviations are also shown), and X^{max} refers to the maximal value. The DREff (in W m^{-2} τ^{-1}) denotes the DRE efficiency. The ftr_DRE denotes the Df-to-total dust ratio (in %,) and δDRE (in % day^{-1}) is the slope of the linear fitting analysis of the hourly averaged ftr_DRE along time, considering a minimum of six ftr_DRE each day.**

		ARN	GRA	EVO	TRJ	BCN
Df	$\overline{DRE}$	-7.1 ± 7.6	-5.9 ± 4.6	-3.8 ± 1.9	-5.9 ± 3.8	-3.1 ± 1.9
	DRE^{max}	-54.1	-28.8	-17.8	-32.5	-27.9
	DREff	-144.2 ± 2.0	-170.3 ± 6.5	-134.5 ± 2.6	-132.9 ± 2.8	-140.4 ± 4.8
Dc	$\overline{DRE}$	-12.2 ± 13.9	-10.4 ± 8.6	-6.3 ± 3.5	-9.6 ± 6.6	-5.2 ± 3.1
	DRE^{max}	-96.3	-52.2	-28.0	-55.4	-41.7
	DREff	-98.4 ± 1.5	-102.9 ± 6.6	-92.0 ± 2.0	-94.0 ± 1.7	-89.0 ± 3.7
DD	$\overline{DRE}$	-19.2 ± 21.4	-16.0 ± 13.2	-10.1 ± 5.4	-15.5 ± 10.3	-8.3 ± 5.0
	DRE^{max}	-150.3	-77.6	-45.9	-87.9	-69.6
	DREff	-111.8 ± 1.5	-120.7 ± 6.8	-104.4 ± 2.1	-105.7 ± 2.0	-103.0 ± 4.0
frt_DRE		38.6	38.0	41.5	38.5	37.6
δDRE		0.62	0.02	0.43	0.77	0.26

675

Table 5: The same as Table 4, but on the top-of-the-atmosphere (TOA).

		ARN	GRA	EVO	TRJ	BCN
Df	$\overline{DRE}$	-5.5 ± 5.6	-4.0 ± 3.7	-2.8 ± 1.6	-4.2 ± 2.8	-2.5 ± 1.6
	DRE^{max}	-35.9	-28.8	-17.7	-23.4	-23.2
	DREff	-103.4 ± 2.8	-119.8 ± 7.6	-105.5 ± 4.1	-92.7 ± 3.6	-114.2 ± 3.9
Dc	$\overline{DRE}$	-7.4 ± 7.8	-5.2 ± 5.8	-3.9 ± 2.8	-5.3 ± 4.2	-3.4 ± 2.2
	DRE^{max}	-53.5	-27.6	-29.2	-35.8	-30.6
	DREff	-57.3 ± 2.2	-57.9 ± 5.0	-61.6 ± 3.5	-52.4 ± 2.8	-58.4 ± 3.2
DD	$\overline{DRE}$	-12.9 ± 13.3	-9.2 ± 9.4	-6.7 ± 4.3	-9.5 ± 7.1	- 6.0 ± 3.7
	DRE^{max}	-85.9	-48.1	-47.1	-58.6	-51.7
	DREff	-70.8 ± 2.3	-74.3 ± 5.6	-74.4 ± 3.6	-64.5 ± 3.0	-73.8 ± 3.3
frt_DRE		43.8	45.5	42.2	44.6	43.3
δDRE		0.55	-2.90	0.67	2.64	0.70

26

680

Table 6: The same as Table 4, but in the atmosphere (ATM).

		ARN	GRA	EVO	TRJ	BCN
Df	$\overline{DRE}$	1.5 ± 2.0	1.9 ± 1.2	1.0 ± 0.5	1.5 ± 1.2	0.6 ± 0.4
	DRE^{max}	22.9	8.9	7.9	12.1	5.1
Dc	$\overline{DRE}$	4.4 ± 6.5	4.9 ± 3.1	2.4 ± 1.2	3.7 ± 2.9	1.8 ± 1.2
	DRE^{max}	60.6	25.7	17.6	26.0	13.3
DD	$\overline{DRE}$	5.9 ± 8.4	6.8 ± 4.2	3.4 ± 1.7	5.2 ± 4.1	2.4 ± 1.6
	DRE^{max}	83.5	33.0	25.6	38.1	18.0
ftr_DRE		27.4	28.5	28.8	29.6	25.0